MNRAS **000**, 1–10 (2021) Preprint 19 May 2021 Compiled using MNRAS LATEX style file v3.0

Towards Realistic Estimates of Solar Global Oscillation Mode-coupling Measurement Noise

M. F. Woodard,[1]⋆
[1] *NorthWest Research Associates, Inc., 3380 Mitchell Lane, Boulder, CO 80301-5410, USA*

Accepted XXX. Received YYY; in original form ZZZ

ABSTRACT

Time series of the medium-l spherical-harmonic decomposition of SOHO/MDI Doppler images were used to investigate the noise of solar-oscillation mode-coupling measurements and to reveal the coupling signatures of global-scale Rossby-waves and magnetic activity. A theoretical model of mode-coupling noise was developed starting from the assumption that the Doppler oscillation signal obeys gaussian statistics. The measured coupling noise was found to agree with the model noise at the level of 20%. The noise of mode-coupling measurements obtained from MDI data turns out to be considerably larger than that of hypothetical, 'ideal' measurements, which could only be obtained from observations with more coverage of the Sun's surface than current instruments provide. The noise analysis was carried out for a simple suboptimal mode-coupling estimation procedure which is described in some detail. A more rigorous, maximum-likelihood, approach to mode-coupling measurement, which generalizes a method currently used to extract global oscillation mode information, is also described and its relationship to the simple mode-coupling analysis is discussed.

Key words: Sun:oscillations – Sun:helioseismology – stars:interiors – convection

1 INTRODUCTION

Large-scale solar mass flows and magnetic fields are not well understood in spite of intense efforts, both observational and theoretical. Flow patterns that have been identified in the Sun include differential rotation, meridional circulation, convection, flows connected with magnetic (sunspot) activity, and, most recently, Rossby waves. Solar magnetic fields are thought to be generated in the 'tachocline', a region of strong shear in the differential rotation near the base of the convection zone. Their organization beneath the photosphere is thought to be influenced by turbulent flow in the outer part of the convection zone.

This paper will focus on the problem of inferring time-varying mass flows and time-varying aspherical structure of magnetic origin from helioseismic measurements. Recent helioseismic observations (Featherstone et al. (2006), Greer et al. (2015), Mandal & Hanasoge (2020, hereafter M20), Woodard (2016, hereafter W16), Nagashima et al. (2020)) have begun to reveal the dynamics of the convection zone, but have yet to yield a consistent or comprehensive picture of the flows there. But it has become clear that Rossby waves are an important component of large-scale solar dynamics (Löptien et al. (2018), Proxauf et al. (2020), M20, Liang et al. (2019)). Seismic measurements of magnetic activity, from large scales down to sunspot scales, indicate that the effects of activity on seismic waves are mainly confined to fairly shallow regions below the photosphere (Libbrecht & Woodard 1990; Braun 1995; Fan et al. 1995; Cally et al. 2016).

Helioseismic mode-coupling analysis is a variant of direct-modeling/statistical-waveform analysis (Woodard 2007), in which oscillation mode-coupling-strength estimates are obtained as an intermediate step in the data analysis. A maximum-likelihood approach was developed by Schou (1992, hereafter S92) to obtain properties, such as frequency and line width, of individual solar p- and f-modes from long sequences of images of the whole solar disk. The S92 method can easily be extended to estimate the couplings of modes of different spherical-harmonic degree l, which are sensitive to steady differential rotation and meridional circulation (Woodard et al. 2013).

As described in Section 2.1, the S92 method can be straightforwardly extended to deal with mode couplings which are sensitive to arbitrary time-dependent mass flows and aspherical magnetic patterns. The connection between the generalized likelihood method and the mode-coupling analysis of W16 (and of M20) is explored in Section 2.2. The data analysis procedure of W16 is motivated and described in Section 2.3. Following this, a quantitative comparison of

⋆ E-mail: mfw@nwra.com

© 2021 The Authors

theoretical and observed mode-coupling noise is described in Section 3.1. A comparison with the noise of 'ideal' helioseismic measurements is also made. Observed mode-coupling signatures of large-scale flow and magnetic-activity patterns are discussed in Section 3.2.

2 GLOBAL-MODE APPROACHES TO HELIOSEISMIC DATA ANALYSIS

2.1 Maximum-likelihood methods

The S92 approach to inferring a set, $\mathbf{x}$, of solar parameters from a set, $\mathbf{y}$, of global solar oscillation data is based on a gaussian likelihood function $L(\mathbf{x},\mathbf{y})$. In the S92 analyses the '$\mathbf{y}$' data are the real and imaginary parts of the spherical-harmonic and frequency-domain (l,m,ω) representation, $\varphi^{lm\omega}$, of a photospheric oscillation observable (e.g., the Doppler velocity) continuously observed over the earth-facing hemisphere of the Sun and over a long span of time. A spherical-harmonic decomposition is appropriate for an approximately spherical and slowly-rotating star, whose oscillation eigenfunctions have an approximately vector-spherical-harmonic form. In its applications to date, the method is tailored to observation spans much longer than the coherence times of oscillation modes of the whole Sun and is appropriate for determining solar properties whose time-variation over the observation span can be neglected.

Following S92, where it is assumed that the solar oscillation signal $\mathbf{y}$ is the realization of a gaussian distribution with zero statistical expectation, we consider likelihood functions of the general form

$$L(\mathbf{x},\mathbf{y}) \propto |\mathsf{E}|^{\frac{-1}{2}} \exp\{-\mathbf{y^T}\frac{\mathbf{1}}{\mathbf{2}\,\mathsf{E}}\mathbf{y}\}, \tag{1}$$

where $\mathbf{y}$ is treated as a vector and 'T' means matrix transpose. We note that the likelihood function depends on the signal only through simple 'covariance' products of the components of $\mathbf{y}$. E is the covariance matrix of the observed signal and $|\mathsf{E}|$ is the absolute value of the determinant of E. Assembling the $\mathbf{y}$ covariance products into the matrix $\mathbf{y}\,\mathbf{y}^T$, we note that

$$\mathsf{E} = \langle \mathbf{y}\,\mathbf{y}^T \rangle, \tag{2}$$

with $\langle .. \rangle$ denoting an average over a hypothetical ensemble of wave fields. The likelihood function depends on the solar parameters $\mathbf{x}$ through the matrix E.

In helioseismic waveform analysis carried out thus far, it has been assumed that flows and magnetic patterns can be treated as small perturbations to a specified reference solar model. Thus standard linear inversion procedures can be used to investigate the perturbations, using covariance products of the oscillation signal as input. The general sensitivity relation for these inversions is based on Equation 2. Waveform analysis has been developed to deal with perturbations, such as turbulent convection and magnetic configurations, which evolve within a given span of data. Such analysis is conveniently carried out in the Fourier ($\mathrm{e}^{-\mathrm{i}\omega\,t}$) domain. One of the consequences of the assumed smallness of the solar perturbations is that covariance products of signal at frequencies ω and ω' are sensitive to fourier components of the solar perturbations of frequencies $\omega' - \omega$ or $\omega - \omega'$. (Note that waveform analysis carried out to date uses the complex-valued coefficients φ^{lm}_{ω} directly, i.e., without separating them into real and imaginary parts.)

The S92 likelihood method has thus far only been used to infer solar properties (e.g, mode frequencies) whose time variation can be ignored on time scales shorter than a dataset. Consequently, in these analyses only covariance data involving signal components of the same frequency need be considered. However, as in waveform analysis, the method can be easily generalized to the study of time-dependent phenomena by including covariance products of distinct frequency components.

For the study of small perturbations about a specified solar reference model, it is useful to define a set of perturbation parameters $\boldsymbol{\xi} \equiv \mathbf{x} - \mathbf{x}_0$, where $\mathbf{x}_0$ are the values of the parameters $\mathbf{x}$ for the reference state. We will assume that small departures from the reference, or zeroth- order, state are linear in the parameters $\boldsymbol{\xi}$. To simplify things further, we consider linear combinations, $\boldsymbol{\eta}$, of the $\mathbf{y}$ data, chosen so that their zeroth-order ($\boldsymbol{\xi} = 0$) covariance matrix is the identity matrix I. We note that, because the E matrix is singular, or at least highly ill conditioned (S92), the dimension of $\boldsymbol{\eta}$ space will in practice be less than that of $\mathbf{y}$ space. For general parameter values we can write

$$\langle \boldsymbol{\eta}\,\boldsymbol{\eta}^T \rangle = \mathsf{I} + \epsilon(\boldsymbol{\xi}), \tag{3}$$

where for sufficiently small perturbations ϵ should be linear in $\boldsymbol{\xi}$. In component form this relation is

$$\langle \eta_i\,\eta_j \rangle = \delta_{ij} + \epsilon_{ij}(\boldsymbol{\xi}). \tag{4}$$

Alternatively, we can write

$$\langle \boldsymbol{\zeta} \rangle = \mathsf{A}\,\boldsymbol{\xi}, \tag{5}$$

where $\boldsymbol{\zeta} \equiv \boldsymbol{\eta}\,\boldsymbol{\eta}^T - \mathsf{I}$ are covariance data minus their zeroth-order expectation and $\mathsf{A} = \partial_{\boldsymbol{\xi}}\,\epsilon$, the parameter-space gradient of ϵ, is the sensitivity matrix of these data. The sensitivity relation can also be written in component form:

$$\langle \zeta_{ij} \rangle = \langle \eta_i\,\eta_j \rangle - \delta_{ij} = \sum_m A_{ij,m}\,\xi_m, \tag{6}$$

where η_i are the components of $\boldsymbol{\eta}$, ξ_m are the components of $\boldsymbol{\xi}$, and $A_{ij,m} = \partial_{\xi_m}\,\epsilon_{ij}$ are the elements of the sensitivity matrix A.

By Bayes' theorem the parameter probability distribution function $P(\boldsymbol{\xi}|\boldsymbol{\eta})$ conditioned on observations $\boldsymbol{\eta}$ is given by

$$P(\boldsymbol{\xi}|\boldsymbol{\eta}) \propto P(\boldsymbol{\xi})\,L(\boldsymbol{\xi},\boldsymbol{\eta}), \tag{7}$$

where $P(\boldsymbol{\xi})$ is the parameter distribution function prior to the observations. We note that, without prior information, the problem of retrieving solar parameters from a helioseismic dataset is usually ill posed. For ease of interpretation we will attempt to represent the updated (posterior) parameter distribution by the gaussian form

$$P(\boldsymbol{\xi}|\boldsymbol{\eta}) \propto \exp\{-(\boldsymbol{\xi} - \hat{\boldsymbol{\xi}})^T \frac{1}{2\,\mathsf{C}}(\boldsymbol{\xi} - \hat{\boldsymbol{\xi}})\}, \tag{8}$$

which is completely defined by the posterior most-probable parameter values $\hat{\boldsymbol{\xi}}$ and their covariance matrix C (the inverse of the so-called Fisher matrix).

To obtain approximate expressions for the posterior parameter statistics $\hat{\boldsymbol{\xi}}$ and C we take the logarithm of Equation 7 using the approximation 8 and expand both sides in

powers of $\boldsymbol{\xi}$. Keeping only the linear and quadratic terms yields

$$-\hat{\boldsymbol{\xi}}^T \frac{1}{\mathsf{C}}\boldsymbol{\xi} + \boldsymbol{\xi}^T \frac{1}{2\,\mathsf{C}}\boldsymbol{\xi} = \mathbf{g}^T\,\boldsymbol{\xi} + \boldsymbol{\xi}^T\,\frac{\mathsf{H}}{2}\,\boldsymbol{\xi}, \tag{9}$$

where $\mathbf{g}$ and H are the parameter space gradient and Hessian matrix, evaluated at $\boldsymbol{\xi} = 0$, of $Q(\boldsymbol{\xi}, \boldsymbol{\eta}) \equiv -\ln(P(\boldsymbol{\xi})) - \ln(L(\boldsymbol{\xi}, \boldsymbol{\eta}))$. The symmetry of $C = C^T$ has been used in obtaining this result. Comparing the two sides of this equation, while noting that H is also a symmetric matrix, leads to the identities

$$\frac{1}{\mathsf{C}} = \mathsf{H}, \tag{10}$$

for the Fisher matrix, and

$$\mathsf{H}\,\hat{\boldsymbol{\xi}} = -\mathbf{g}, \tag{11}$$

for the most probable $\boldsymbol{\xi}$ values. We note that the accuracy of the above result depends on the validity the gaussian approximation Equation 8.

2.2 Connection between likelihood and waveform analysis

The gradient and Hessian, $\mathbf{g}$ and H, are each the sum of a 'P' term and an 'L' term, respectively contributed by the prior probability function and the likelihood function. Thus Equations 10 and 11 can be rewritten

$$\frac{1}{\mathsf{C}} = \mathsf{H}(P) + \mathsf{H}(L) \tag{12}$$

and

$$[\mathsf{H}(P) + \mathsf{H}(L)]\,\hat{\boldsymbol{\xi}} = -\mathbf{g}(P) - \mathbf{g}(L). \tag{13}$$

These equations show how the posterior estimate of $\boldsymbol{\xi}$ depends on the data-dependent gradient $\mathbf{g}(L)$ and Hessian $\mathsf{H}(\mathsf{L})$, for arbitrary prior information, encoded in $\mathsf{H}(\mathsf{P})$ and $\mathbf{g}(P)$.

The elements of the derivation of $\mathbf{g}(L)$ and $\mathsf{H}(L)$ are given in S92 and will not be repeated here. For the gradient we obtain

$$\mathbf{g}(L) = \frac{-1}{2}\,\mathsf{A}^T\,\boldsymbol{\zeta}, \tag{14}$$

where $\boldsymbol{\zeta}$ is the vector of covariance products and A is their parameter sensitivity matrix that were defined in the context of Relation 5. Similarly, we find that the Hessian has the form

$$\mathsf{H}(\mathsf{L}) = \frac{1}{2}(\mathsf{A} + \mathsf{Z})^T\,\mathsf{A}, \tag{15}$$

where $Z_{jk,m} \equiv 2\sum_i \zeta_{ij}\,A_{ik,m}$. By analogy with Equation 13, the most probable value, $\hat{\boldsymbol{\xi}}(L)$, of the likelihood function obeys $\mathsf{H}(L)\,\hat{\boldsymbol{\xi}}(L) = -\mathbf{g}(L)$. And from Equations 14 and 15 we further obtain

$$(\mathsf{A} + \mathsf{Z})^T\,\mathsf{A}\,\hat{\boldsymbol{\xi}}(L) = \mathsf{A}^T\,\boldsymbol{\zeta}. \tag{16}$$

Were it not for the data-dependent matrix Z, this relation would have the form of the adjoint equation of a linear least-squares fitting problem. Least-squares fitting was the basis for a previous analysis of mode-coupling measurement noise (Woodard 2014, hereafter W14). In principle, the maximum-likelihood method should yield less noisy mode-coupling measurements than the least-squares method.

2.3 Measuring mode-coupling parameters

We now consider the application of the foregoing parameter estimation method to the problem of determining oscillation mode coupling strengths, which are sensitive to interior properties of interest. As a preliminary step in formulating the statistics of realistic oscillation datasets, we first consider, as in W14, the statistics of the wave field within the entire volume of the Sun over a long span of time. Then we go on to discuss the analysis of realistic data, which significantly undersample the wave field.

The wave field is represented by the amplitudes a^i_ω which give the frequency dependence of the magnitude and phase of individual normal oscillation modes of the zeroth order model. Because of the near spherical symmetry of the model the mode indices i are radial and spherical-harmonic indices $i = n, l, m$. Since the solar differential rotation is reasonably well known, largely from helioseismic observations, the zeroth-order model would ideally be a differentially rotating one with all the effects of rotation (and perhaps meridional circulation) on the wave field embodied in the zeroth-order statistics of the oscillation signal, which for the time being is the wave field. Nevertheless, as in W16 and M20, we continue to ignore the effect of differential rotation on the spherical-harmonic form of the mode eigenfunctions. This neglect is probably not terribly important for wave modes of l less than 150, an analysis of which will be described in what follows. But deviations from spherical-harmonic form certainly become apparent at larger l. On the other hand, we do include the effect of rotationally split eigenfrequencies on the zeroth-order wave-field statistics.

For ideal observations, the y data are the real and imaginary parts of the amplitudes a^i_ω. The y-data covariance matrix E can be straightforwardly constructed from the set of second moments $\langle a^j_{\omega'}\,a^i_\omega\rangle$ and $\langle a^j_{\omega'}\,a^{i*}_\omega\rangle$ of the mode amplitudes. W14 assumed that in zeroth-order the solar wave field is the realization of a time-stationary and isotropic random process, with the consequence that the statistics of the mode amplitudes of different l, m, ω are mutually independent with random phases, aside from the small correlations implied by mode coupling. A further consequence is that for fixed (n, l) the zeroth-order amplitude power density $\langle|a^{nlm}_\omega|^2\rangle_0$ is the same function of $\omega - \omega_{nlm}$ at each m, where the ω_{nlm} are the rotationally split mode eigenfrequencies. (In a more realistic statistical model, the assumed isotropy of mode excitation and damping would be broken by the advection of turbulent wave sources by the differential rotation.)

For the remainder of this paper, we consider couplings only of modes of the same radial order and generally suppress the index n. Thus the zeroth-order wave-field statistics of modes can be summarized by

$$\langle a^{l'm'}_{\omega'}\,a^{lm}_\omega\rangle_0 = 0 \tag{17}$$

and

$$\langle a^{l'm'}_{\omega'}\,a^{lm\,*}_\omega\rangle_0 = \langle|a^{lm}_\omega|^2\rangle_0\,\delta_{l'l}\,\delta_{m'm}\,\delta_{\omega'\omega} \tag{18}$$

in which 'δ' denotes the Kronecker symbol. The statistical independence of distinct frequency components of the wave field, implied by the above factor $\delta_{\omega'\omega}$, holds only in the limit of long spans of data. Since physical wave fields are real valued, the mode amplitudes at $(l, -m, -\omega)$ and (l, m, ω) are re-

dundant information for spherical-harmonic eigenfunctions. In this case we can ignore negative-frequency mode amplitudes.

For a differentially-rotating reference model, it seems likely that the $\delta_{l'l}$ factor in the last equation would have to be modified, to include the effect of the mode driving and damping anisotropies. (The $\delta_{m'm}$ factors, which reflect the axisymmetric nature of the differential rotation in the shallow subphotospheric layer where waves are emitted and absorbed, would remain.) Alternatively, these anisotropies could be treated as perturbations, though in this paper we treat only time-dependent perturbations.

Time-dependent and aspherical perturbations couple the amplitudes of different reference modes in the sense that they produce correlation between general mode amplitudes a_ω^{lm} and $a_{\omega'}^{l'm'}$. Thus

$$\langle a_{\omega'}^{l'm'}\, a_\omega^{lm\,*}\rangle = \langle a_{\omega'}^{l'm'}\, a_\omega^{lm\,*}\rangle_0 + \delta\langle a_{\omega'}^{l'm'}\, a_\omega^{lm\,*}\rangle, \tag{19}$$

where an isotropic form for the zeroth-order term is given by Equation 18 and the perturbation term $\delta\langle a_{\omega'}^{l'm'}\, a_\omega^{lm\,*}\rangle$ quantifies the correlations.

Approximate expressions for $\delta\langle a_{\omega+\sigma}^{l'm'}\, a_\omega^{lm\,*}\rangle$ were given in W16, based partly on Lavely & Ritzwoller (1992), in the weak-coupling (Born) approximation, for various physical perturbations. The expressions are proportional to complex-valued coupling 'strengths', $\lambda_{lm}^{l'm'}(\omega'-\omega)$, which quantify the effect of perturbations. For fixed l, l', t, and σ, where $(t,\sigma) = (m'-m, \omega'-\omega)$, the coupling strengths can be expanded in a set of orthonormal functions of m, yielding a set of expansion coefficients $b_{s,\sigma}^t(l,l')$ which are sensitive to individual spherical-harmonic (s,t) and frequency (σ) components of perturbed quantities. The b coefficients could be obtained individually from wave field data, by analogy with the extraction of 'a' (frequency-splitting) coefficients from spherical-harmonic-frequency spectra (e.g., S92). Actual data analysis is complicated by mode leakage, as described below, and by the fact that reference eigenfunctions depart more and more from their nominally spherical-harmonic form with increasing l.

Our immediate interest is in probing perturbations of much larger angular scale and longer time scale than the scales of the waves serving as probes. Thus in what follows we take (s,t,σ) values to be somewhat smaller in magnitude than the magnitudes of typical (l,m,ω) or (l',m',ω') combinations. We have ignored the perturbation of $\langle a_{\omega'}^{l'm'}\, a_\omega^{lm}\rangle$, which by Equation 17 has no zeroth-order contribution. Since $a_\omega^{lm} = (-1)^m\, a_{-\omega}^{l,-m\,*}$ (using appropriate spherical-harmonic sign conventions) the neglected expectation value has the same form as the perturbation terms discussed above that are sensitive to coupling parameters $b_{s,\omega+\omega'}^{m+m'}$. Since ω and ω' are positive by our convention these terms are sensitive to much more rapid changes than interest us here.

Because existing observations do not sample the entire wave field, the coefficients φ_ω^{lm} we obtain from helioseismic image sequences are superpositions of mode amplitudes. The weighting of different modes is given by a leakage relation of the form

$$\varphi_\omega^{lm} = \sum_{l'm'} L_{l'm'}^{lm}\, a_\omega^{l'm'}. \tag{20}$$

Leakage in l and m is an artifact of observations that cover only the half of the Sun's surface visible from near the Earth. So leakage could be reduced by future, 'whole-sphere' observations, obtained from multiple vantage points. On the other hand, modes of different n contribute to each φ_ω^{lm} because waves are only observable near the photosphere. Thus, even whole-sphere observations only approximate ideal observations.

For full-disk observations the leakage matrix is dominated by elements for which (l,m) and (l',m') differ by small integers. The above expression is suitable for observations obtained by a spacecraft moving in a circular orbit about the Sun in the solar equatorial plane. The orbits of real instruments or observatories are typically not quite circular and are a bit inclined to the Sun's equator. Therefore the true leakage matrix, being time dependent, would involve a convolution in frequency in addition to the indicated transformation in wave number (l,m). This would also be the case if there were significant gaps in the oscillation time series. For the time being, however, we continue to use the time-independent leakage relation 20 for the analysis of helioseismic data.

With the help of the preceeding equation, we obtain expressions, analogous to Equations 17, 18, and 19, for the expectations of general covariance products. As with mode-amplitudes, only cross-spectral ($\omega' = \omega$) products of φ_ω^{lm} have zeroth-order expectations. Therefore, for strictly time-dependent ($\sigma = \omega' - \omega \neq 0$) perturbations, $\delta\langle\varphi_{\omega'}^{l'm'}\varphi_\omega^{lm\,*}\rangle$ is just $\langle\varphi_{\omega'}^{l'm'}\varphi_\omega^{lm\,*}\rangle$ and is a superposition of many mode-coupling strengths, a circumstance which complicates the task of extracting individual b coefficients. The complication is a further consequence of mode leakage. The problem of retrieving b parameters from helioseismic data is equivalent to the problem of mapping time-varying aspherical structure within the solar interior. Since the globally-coherent waves we observe on the Sun's Earth-facing hemisphere carry information about conditions on the far hemisphere, b-coefficient leakage is expected to be less severe than mode-amplitude leakage. Indications of how well the changing aspherical structure of the solar interior can be mapped using oscillation data come from helioseismic imaging of the Sun's far hemisphere (Lindsey & Braun 2000).

Henceforth, we focus on the problem of estimating the coupling parameters $b_{s,\sigma}^t(n,l)$ of modes of the same l, as well as n, for which measurements exist (W16, M20). For insight into the analysis of actual data we first consider how ideal data would provide information about mode couplings. For statistically independent mode amplitudes, the likelihood function L for these b parameters is a product of functions L_{nl} each depending on the b parameters and amplitude data of one (n,l) multiplet. In consequence the Hessian $\mathsf{H}(L)$ of $-\ln(L)$ is a sum of terms, as in Equation 15, each dependent on the b parameters and mode amplitudes of one multiplet. One can, as usual, improve the statistics of b measurements, $\hat{b}_{s,\sigma}^t(n,l)$, by averaging them over ranges of n and l, though at the expense of n and l resolution, which in solar model terms implies a loss of depth resolution.

As discussed in W16, averaging the *signed* b measurements over n and l will increase the detectability of solar flows and other subsurface structures that are coherent over great ranges of depth. Since the Hessian of n- and l-averaged parameters is the sum of the Hessians of the multiplets involved in the averaging, we expect that, with enough averaging, the data-dependent (Z) terms in the Hessians can ef-

fectively be replaced by their expectation values. Combining the expression given in the discussion of Equation 15, with Equation 6, we find that the Z term has no zeroth-order expectation. Thus it is appropriate to use the least-squares (Z = 0) form of the Hessian if only coarse depth resolution is needed.

The W16 and M20 global mode-coupling analyses of large-scale time-variable flows and magnetic activity are based on suboptimally-weighted least-squares procedures in which b coefficients are separately fitted to helioseismic covariance data of the appropriate mode multiplet. The estimate of $b^t_{s,\sigma}(n,l)$ used in W16 has the form

$$\hat{b}^t_{s,\sigma} = \sum_{m\omega} g^{st,\sigma\,*}_{m\omega}\, \varphi^{m+t}_{\omega+\sigma}\, \varphi^{m\,*}_{\omega}. \tag{21}$$

An expression for the weight function $g^{st,\sigma\,*}_{m\omega}$ is given in W16 along with a precise but not entirely correct description of the $m-\omega$ domain involved in the above summation. To clarify matters we note that the magnitude of the weight function is dominated by a pair of narrow ridges, centered at $\omega = \omega_m$ and at $\omega+\sigma = \omega_{m+t}$, for each physically meaningful value of m. This structure reflects the time-dependent nature of the coupling of mode pairs within the multiplet. The summation domain of Equation 21 is simply the vicinity of the resonant ridges. It is well to keep in mind that, for near-Earth-based observations, ω and σ in the above expressions are synodic frequencies.

The $\hat{b}^t_{s,\sigma}$ statistic is sensitive not only to the target $b^t_{s,\sigma}$ parameter of one mode multiplet, but to other b parameters, including those of other multiplets. A leakage relation, analogous to Equation 20, for the sensitivity of $\hat{b}^t_{s,\sigma}$ to other b parameters can be derived first by taking the expectation value of Equation 21. The expectations $\langle \varphi^{m+t}_{\omega+\sigma} \varphi^{m\,*}_{\omega} \rangle$ that appear on the right side of the resulting equation are then replaced, using Equation 20, by mode-amplitude covariances, given by Equation 19. For non-zero σ, the latter covariances have no zeroth-order perturbation and can be expressed in terms of b coefficients as noted in the discussion of Equation 19. The resulting b-coefficient leakage relation serves to define a linear inverse problem for the b parameters.

To complete the definition of the inverse problem we need the covariance matrix of the $\hat{b}$ statistics. The covariance matrix of the real and imaginary parts of the b-parameter estimates of a single mode multiplet is obtainable from the covariances $\mathrm{cov}(\hat{b}^{t'}_{s',\sigma'}, \hat{b}^t_{s,\sigma})$ and $\mathrm{cov}(\hat{b}^{t'}_{s',\sigma'}, \hat{b}^{t\,*}_{s,\sigma})$, where $\mathrm{cov}(w,z)$ of two complex random variables has the usual meaning $\langle wz\rangle - \langle w\rangle\langle z\rangle$. These covariances involve fourth moments of the oscillation signal, which in the gaussian approximation can be reduced to products of second moments, as discussed in Appendix C of Gizon & Birch (2004). Ignoring perturbation terms, the b covariances of interest can therefore be expressed as sums over products of cross spectra. For strictly positive σ and σ', the only non-zero b covariances turn out to be

$$\mathrm{cov}(\hat{b}^{t'}_{s',\sigma}, \hat{b}^{t\,*}_{s,\sigma}) = \sum_{m'm\omega} g^{s't',\sigma\,*}_{m'\omega}\, g^{st,\sigma}_{m\omega}\, \langle \varphi^{m'+t'}_{\omega+\sigma}\, \varphi^{m+t\,*}_{\omega+\sigma} \rangle \langle \varphi^{m'\,*}_{\omega}\, \varphi^{m}_{\omega} \rangle. \tag{22}$$

3 OBSERVATIONAL ANALYSIS

3.1 Tests of the helioseismic statistical model

In W14 theoretical estimates of mode-coupling noise were obtained for ideal data, with statistics given by Equations 17 and 18. So it is of interest to estimate the coupling measurement noise of existing helioseismic data and compare it with that of ideal measurements. One would also like to test the noise model. For this test we compare the noise of existing b-coefficient measurements with theoretical expectations. We note that the $\hat{b}^t_{s,\sigma}$ statistic is a suboptimally-weighted least-squares estimate of the solar parameter $b^t_{s,\sigma}$ and is constructed only from covariance data which are particularly sensitive to the true parameter.

The current study uses b coefficients computed from MDI spherical -harmonic time series (Scherrer et al. 1995; Larson & Schou 2015) based on the algorithm more or less as described in W16, but clarified in the above discussion of Equation 21. Coefficients were computed for all spherical-harmonic components of positive s and t up through $s = 10$ for 720-day epochs within the overall $\approx$ 15-year time span of MDI observations. The b coefficients obtained from the first 720-day epoch of MDI data were used in the initial set of statistical tests presented below.

As a simple test of the statistical model, we compare observed and theoretical b-coefficient 'power', for various combinations of n, s, and t. For this test, power is defined to be $|\hat{b}^t_{s,\sigma}(n,l)|^2$. As noted in the discussion of Equation 21, the $\hat{b}^t_{s,\sigma}(n,l)$ statistic has a non-zero expectation linearly dependent on mode-coupling parameters. Due to the weakness of the couplings under consideration, the expectation value is much smaller in magnitude than the noise and we can compute the expected value of b-coefficient power from $\mathrm{cov}(\hat{b}^t_{s,\sigma}(n,l), \hat{b}^{t\,*}_{s,\sigma}(n,l))$ using Equation 22. As the $\hat{b}$ statistic is very noisy, many samples of $|\hat{b}|^2$ need to be averaged to provide statistically significant comparisons with theory. Consequently we compare observed and expected b-coefficient power averaged over ranges of σ or l.

We begin by considering b-coefficient power obtained by averaging over σ. The resulting power could be plotted (for fixed n, s, and t) as a function of l. However, motivated by the theoretical result of W14 that b-coefficient power is ideally proportional to mode line width, we instead plot the dependence on line width (i.e., the full width at half maximum power density). Figure 1 shows the width dependence of both theoretical and observed power for a sampling of (n,s,t) combinations. As the measurement is not optimal, it should not be surprising that the dependence of observed and theoretical power shows some deviation from linearity. Following the discussion of W14, the theoretical noise power of ideal b-coefficient measurements is $\gamma\,\Delta\omega/4\pi$, where γ is the mode line width and $\Delta\omega$ is the frequency resolution of the observation span, both in radians/sec. As seen in Figure 1, the observed power is considerably larger than this. (It should be noted that b coefficients have the dimensions of angular velocity in c.g.s units. Therefore, power has units of radians^{2}sec^{-2}.)

Next we consider frequency-dependent power obtained from l averaging. For this step, l-dependent weights, inversely proportional to the mode line widths, were used to obtain averages. Examples are shown in Figure 2. The the-

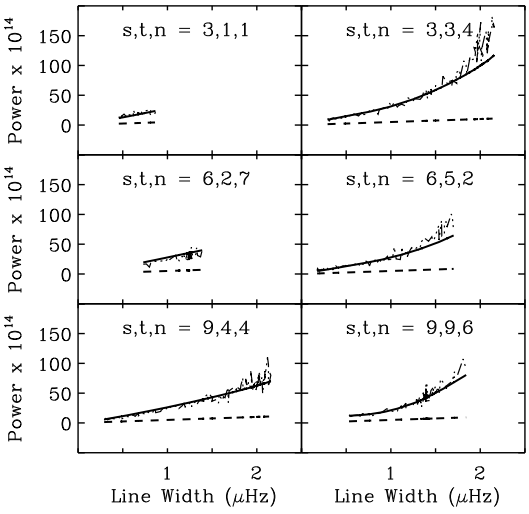

Figure 1. Line width dependence of b-coefficient power, for several n, s, and t combinations, as discussed in Section 3.1. The solid lines are theoretical expections and the broken lines are estimates computed from MDI data. The dashed lines are the theoretical expectations for ideal data. In this and other figures, b-coefficient power is in units of radians^{2}sec^{-2}.

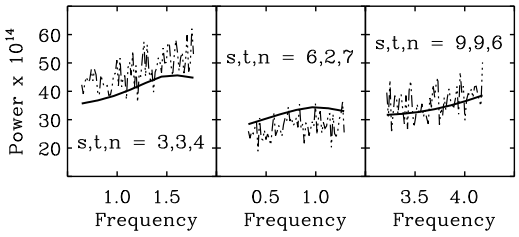

Figure 2. Frequency dependence of l-averaged b-coefficient power, for a few n, s, and t combinations, as described in Section 3.1. As in Figure 1, frequency is given in μHz and the solid and broken lines are respectively theoretical expections and observations.

oretical curves broadly agree with the observations, though systematic discrepancies of order 20 percent are apparent. (We note that the σ range plotted for each t value was chosen to target large-scale solar perturbations rotating at roughly the solar rotation rate.)

To test the statistical model more fully, we estimate the covariances $\mathrm{cov}(\hat{b}', \hat{b}*)$ and $\mathrm{cov}(\hat{b}', \hat{b})$ of the observed coefficients $b \equiv b^t_{s,\sigma}(n,l)$ and $b' \equiv b^{t'}_{s',\sigma+\delta\sigma}(n,l)$, as a function of frequency lag $\delta\sigma = \sigma' - \sigma$, for general s, t, s', t' values. For this exercise, it is convenient to work with dimensionless b coefficients, β, defined for arbitrary indices by $\hat{\beta} = \hat{b}/\sqrt{\langle|\hat{b}|^2\rangle}$. Using the above shorthand notation, we note that the discussion of Equation 22 implies that $\mathrm{cov}(\hat{\beta}', \hat{\beta})$ is expected to vanish for all frequency lags $\delta\sigma$, while $\mathrm{cov}(\hat{\beta}', \hat{\beta}*)$ is also expected to vanish except at zero lag. The theoretical values of general covariances $\mathrm{cov}(\hat{\beta}', \hat{\beta}*)$ at zero lag were not computed for this study. But the β coefficients are normalized so that the covariance in question is unity for the cases $s', t' = s, t$. For ideal data, this covariance is the only non-zero one, but mode leakage is expected to introduce analogous leakage between b measurements, as noted in the discussion of Equation 21.

Figure 3 shows cross-covariance functions $\mathrm{cov}(\hat{\beta}', \hat{\beta})$ and $\mathrm{cov}(\hat{\beta}', \hat{\beta}^*)$ derived from MDI data averaged over the observed l range for $s = 5$, $t = 3$, and $n = 6$ for several s', t' combinations. Excepting the real parts of $\mathrm{cov}(\hat{\beta}', \hat{\beta}^*)$ at zero-lag, all the correlation functions vanish, aside from what appear to be small random fluctuations, as expected. For the $(s', t') = (s, t)$ (power spectral) case, the value of the dominant peak is reasonably close to the theoretical value unity, while the dominant peaks for the non-spectral cases are somewhat smaller than unity, as one might expect from a leakage effect.

Figure 4 shows measured β cross covariance functions for two additional combinations of s' and t'. Unlike the functions shown in Figure 3, the functions shown here do not contain strong peaks, illustrating the general weakness of the cross talk between perturbations of opposite reflection symmetry across the solar equator. The $\mathrm{cov}(\hat{\beta}', \hat{\beta}^*)$ covariance functions displayed here do show possibly significant, though small, deviations from theoretical expections, in the form of troughs at the second harmonic of the fundamental frequency of the 720-day span of the analyzed time series. This period is of course suspiciously close to the inverse of Earth's orbital period. The discussion of the leakage matrix (defined by Equation 20) suggests that such anomalies could be a consequence of our having ignored the inclination of the solar rotation axis to the ecliptic axis and the non circularity of the Earth's orbit in modeling mode leakage.

The cross covariance functions shown thus far involve b coefficients of odd s. These coefficients are ideally sensitive to components of the Sun's large-scale toroidal velocity field (Lavely & Ritzwoller 1992; Hanasoge et al. 2017). In contrast, the curves shown in Figure 5 are measurements of the cross talk between b coefficients of even and odd s and the latter are mainly sensitive to magnetic activity. As expected for spherical-harmonic functions of opposite reflection symmetry, these covariances are again fairly weak, indicating that the helioseismic problems of characterizing magnetic and velocity information are highly decoupled in spite of mode leakage.

A cross-covariance analysis analogous to the preceeding ones was also performed by interchanging the roles of l and σ. The conclusion of the analysis (not shown) is that the

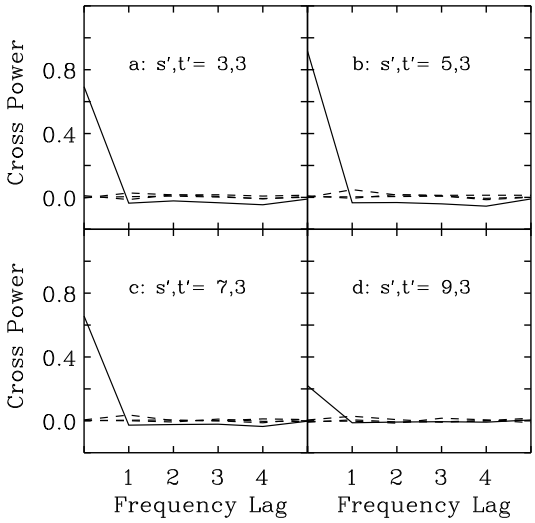

Figure 3. Cross-covariance functions involving the dimensionless b coefficients, β, at $s = 5$, $t = 3$, and for various combinations of s' and t'. The solid lines in each panel are the real parts of the function $\mathrm{cov}(\hat{\beta}', \hat{\beta}^*)$, while the imaginary part of the function together with the real and imaginary parts of the function $\mathrm{cov}(\hat{\mathrm{b}}', \hat{\mathrm{b}})$ are shown as dashed lines. The unit of the frequency axis is the inverse of 720 days.

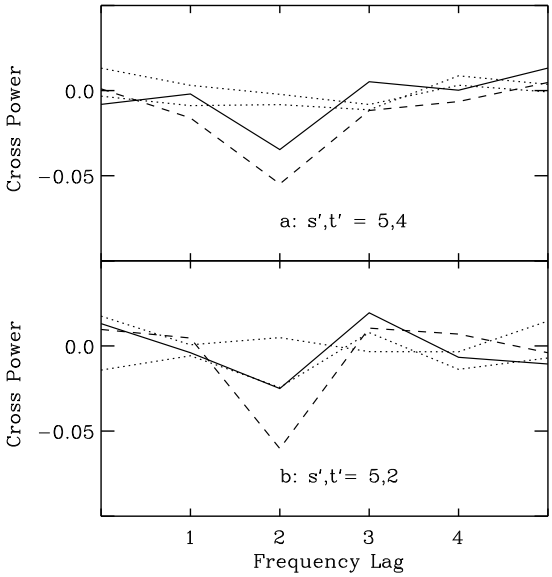

Figure 4. Covariance functions of the type shown in Figure 3, for two combinations of s' and t'. The solid and dashed curves are respectively the real and imaginary parts of $\mathrm{cov}(\hat{\beta}', \hat{\beta}*)$, while the dotted curves represent the $\mathrm{cov}(\hat{\beta}', \hat{\beta})$ function. Note that the vertical scale here differs from that of Figure 3.

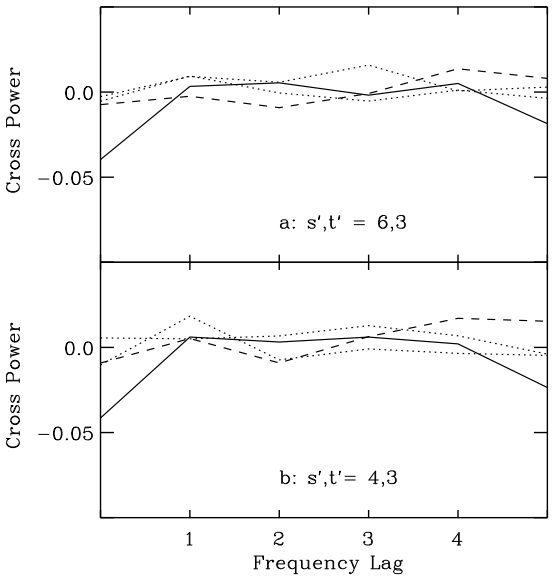

Figure 5. Covariance functions illustrating velocity-magnetic crosstalk, as described in the text. The plotting conventions here are identical to those of Figure 3

b coefficients of mode multiplets of different l are uncorrelated. The lack of correlation (i.e., the absence of leakage) in l is expected for ideal data but has no obvious explanation for real data. It should be interesting to see if the result is consistent with the statistical model, but the relevant calculations have yet to be carried out. An alternative way of confirming the statistical independence of b measurements of different l is to compute the power of the observed b coefficients summed over l. More precisely, we define $\zeta^t_{s,\sigma}(n)$ to be $\beta^t_{s,\sigma}(n, l)$ summed over the observed l range and divided by the square root of the number of samples. If the samples are independent, the expected value of the power $|\zeta^t_{s,\sigma}(n)|^2$ is unity. The top panel of Figure 6 shows the observed cross-covariance function $\mathrm{cov}(\zeta^t_{s,\sigma+\delta\sigma}(n), \zeta^{t\,*}_{s,\sigma}(n))$, averaged over the observed range of n, s, and t. As expected, the curve is dominated by a peak at zero lag of unit magnitude. Also shown in this panel is the auto-covariance function $\mathrm{cov}(\zeta^t_{s,\sigma+\delta\sigma}(n), \zeta^t_{s,\sigma}(n))$, whose expectation value vanishes according to the noise model. The bottom panel of the same figure also shows the measured auto-covariance function $\mathrm{cov}(|\zeta^t_{s,\sigma+\delta\sigma}(n)|^2, |\zeta^t_{s,\sigma}(n)|^2)$ averaged over indices. A predominant peak at zero lag is again expected, confirming once again the statistical independence of the wave field at different frequencies. The theoretical value of the power at zero frequency lag is not yet available for comparison.

3.2 Global-mode-coupling signatures of large-scale flows and magnetic activity

Having concentrated on noise in the previous Section, we now give a brief overview of the observable signatures of large-scale flow velocities and of magnetic activity. For the analysis of noise we ignored the contribution of these signatures to the statistics of individual b-coefficient estimates on the grounds that the contributions are much smaller

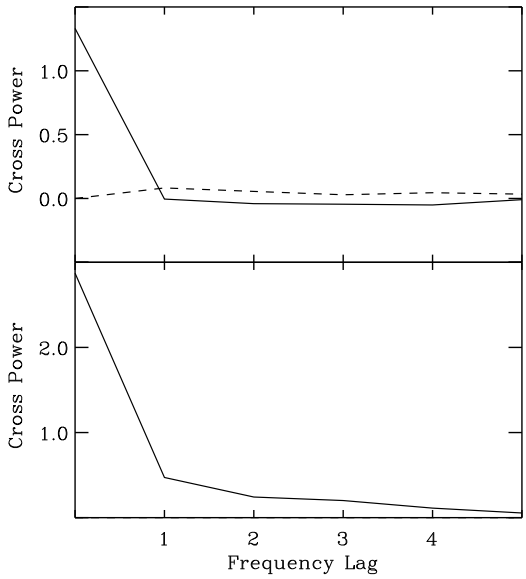

Figure 6. The top panel shows the observed cross-covariance function $\mathrm{cov}(\zeta^t_{s,\sigma+\delta\sigma}(n), \zeta^{t\,*}_{s,\sigma}(n))$, averaged over the observed range of n, s, and t. Also shown in this panel is the auto-covariance function $\mathrm{cov}(\zeta^t_{s,\sigma+\delta\sigma}(n)\, \zeta^t_{s,\sigma}(n))$, whose real and imaginary parts are shown as solid and dashed curves, respectively. The bottom panel shows the measured (positive-valued) auto-covariance function $\mathrm{cov}(|\zeta^t_{s,\sigma+\delta\sigma}(n)|^2, |\zeta^t_{s,\sigma}(n)|^2)$ averaged over indices.

than the noise. As noted in W16, the signal-to-noise ratio of the b-coefficient signatures of large-scale flows and solar activity can be improved by averaging or smoothing the n and l dependence of the signed coefficient measurements $(-1)^l\, \hat{b}^t_{s,\sigma}(n,l)$, yielding coefficients $\hat{\xi}^t_{s,\sigma}$. The $s-t-\sigma$ power spectrum $|\xi^t_{s,\sigma}|^2$ also contains a substantial noise contribution, though the statistical uncertainty of this contribution decreases with increasing volumes of solar data. The noise contribution to $|\xi^t_{s,\sigma}|^2$ was estimated from $|\eta^t_{s,\sigma}|^2$, where $\eta^t_{s,\sigma}$ is formed in a similar way to $\xi^t_{s,\sigma}$, from *unsigned* b coefficients. The η coefficients are essentially pure noise because the coupling sensitivity of the b coefficients changes rapidly with l. (Alternatively, the noise contribution could be computed theoretically, following the discussion of Equation 22.)

To display the mode-coupling signatures of solar perturbations, the entire $\approx$ 15-year span of MDI spherical-harmonic time series was divided into eight high-duty-cycle, minimally overlapping 720-day series, and from each subseries b-coefficients were computed according to Equation 21. Coupling coefficients were computed for all positive t for each s between 1 and 10 inclusive and for narrow s- and t-dependent σ ranges chosen to track rotating solar velocity and magnetic features. The computation was carried out for all (n,l) multiplets in the angular wavenumber and frequency ranges $30 < l < 150$ and $1.5 < \nu(\mathrm{mHz}) < 3.5$.

The odd-s b coefficients are sensitive to toroidal flows, while the even-s coefficients are sensitive to magnetic activity. As indicated in Section 3.1, there is relatively little leakage between the velocity and magnetic coefficients. For the present flow analysis the $\xi^t_{s,\sigma}$ coefficients are simple averages of the signed b coefficients over ranges of $l_0 \equiv 3\, l/\nu(\mathrm{mHz})$. (We note that p modes of the same l_0 have depth sensitivity to perturbations of large depth range similar to p modes of degree l_0 and frequency 3 mHz.) The results described below focus on the l_0 range 150 through 250. Power spectra $|\xi^t_{s,\sigma}|^2$ were computed for each of the 720-day epochs and then averaged over the eight chosen MDI epochs, yielding a time-averaged $s-t-\sigma$ spectrum.

The time-averaged spectra confirm the findings of Löptien et al. (2018) that much of the large-scale flow velocity power, attributed by W16 to turbulent convection, is in fact due to Rossby wave motions. Thus far, only sectoral $(s = t)$ Rossby modes have been identified in the Sun. Figure 7 shows time-averaged sectoral frequency spectra $|\xi^t_{t,\sigma}|^2$. The frequency scale of the plots has been translated so that patterns rotating at the nominal sidereal equatorial rate of 453.1 nHz would show up at zero frequency. With the full set of MDI data, the sectoral Rossby-mode peaks are statistically very significant and their frequencies are consistent with the Loptien *et al.* measurements, which agree with the approximate theoretical dispersion relation

$$\omega = -2t\Omega/[s(s+1)], \tag{23}$$

of modes of a star rotating rigidly at sidereal rate Ω. The frequencies ω pertain to the frame corotating with the star. The solar Rossby-mode observations are consistent with the above-quoted sidereal rate. (We note that the $s = 1$ mode frequency falls outside the range of the present analysis.)

With hindsight, we see that Rossby-modes can be identified in mode-coupling measurements based on only two years of helioseismic data (M20). We see that, away from the Rossby peaks, the power $|\hat{\xi}^t_{s,\sigma}|^2$ tends to agree with the estimated noise power $|\xi^t_{s,\sigma}|^2$. The total (frequency-integrated) power of individual Rossby peaks, when ξ-coefficient power is converted to absolute velocity power according to Equation 12 of W16, is in rough agreement with the meter-per-second mode velocity amplitudes inferred by other observers (Löptien et al. (2018), M20).

For each observed t value, the $s = t+2$ mode-coupling spectra also show a peak at the frequency of the $s = t$ Rossby-mode. This leakage could be a manifestation of the non-spherical-harmonic (symmetry-breaking) nature of the Rossby modes (as detailed in Proxauf et al. (2020)), but to some extent must also be a consequence of observational leakage (e.g., Figure 3). The latter leakage needs to be better quantified. Due to approximate symmetries about the solar equator (on the one hand, of the solar angular velocity, and on the other, of observational sensitivity) leakage of odd-s sectoral Rossby-modes into even-t spectra is expected to be small. Nevertheless, there are suggestions in the even-t spectra of approximately corotating, presumably non-Rossby-wave, velocity features.

To improve the visibility of corotating features, 'derotated' time-averaged spectra of velocity features were averaged over odd s and even t. The resulting composite, shown in the bottom panel of Figure 8, contains a statistically significant peak due to approximately corotating velocity patterns. Corotating velocity power was previously detected by Liang et al. (2019) at low t, where it was noted that possible contributors to this power include turbulent motions and motions connected with active regions. Interestingly, the sectoral spectra (Figure 7), in which the Rossby-mode peaks are prominent, seem to be deficient in corotating velocity

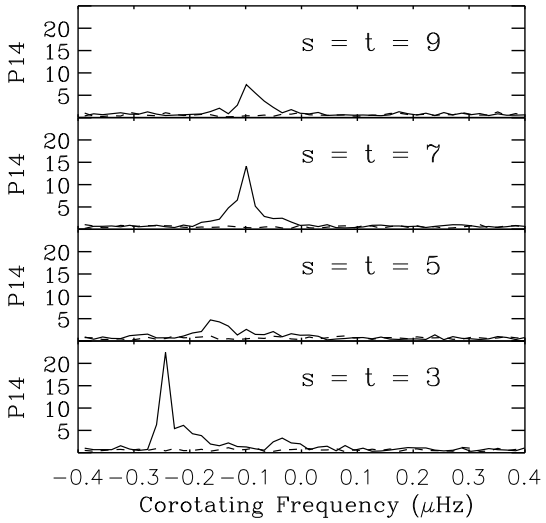

Figure 7. Large-scale velocity power $|\xi^t_{s,\sigma}|^2$ averaged over the ≈ 15-year span of MDI observations, dominated by Rossby-mode peaks, as described in the text. For comparison, the dashed curve is the analogous average of the estimated noise power $|\eta^t_{s,\sigma}|^2$, described in Section 3.2. In this Figure 'P14' denotes b-coefficient power times 10^{14}. The frequency scales of this and the remaining plots have been translated to simulate observations obtained in a corotating frame.

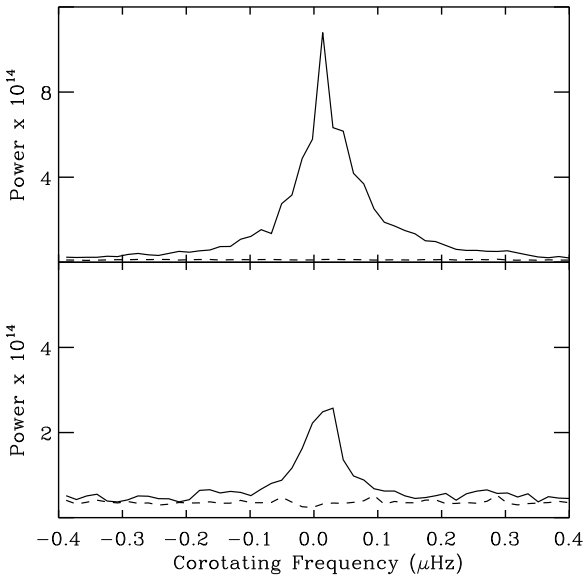

Figure 8. Composites of de-rotated large-scale mode-coupling power spectra, as described in the text. The bottom panel shows velocity features, while the top panel shows magnetic-activity features. The dashed curves are noise power analogous to the dashed curves of Figure 7. Note the difference between the vertical scales of the top and bottom panels.

power. We also note that, when the foregoing analysis of large-scale velocity power is repeated with p modes of lower l_0, the signal-to-noise ratio of the inferred velocity features (both Rossby-modes and corotating features) is much less than for the cases shown.

The presence of Rossby-mode oscillations complicates the detection of other large-scale flows, such as convection. According to Equation 23 the Rossby-mode peaks may be difficult to distinguish from (toroidal) convective contributions for s greater than about 10, as convective patterns are expected to be roughly corotating. Although we cannot rule out 'contamination' by non-sectoral Rossby waves, one might look for convective patterns in non-sectoral components of the flow velocity. Yet another way to discriminate Rossby waves from convection might be to examine the degree of correlation between the inferred flow velocity at different depths, as velocity patterns with a cellular structure would be expected to show less vertical coherence than a global wave mode. Whether current data are of sufficiently high signal-to-noise to distinguish different kinds of flow patterns is not clear, however. On the other hand, convective flows, unlike Rossby waves, are expected to have a poloidal, as well as a toroidal, component. Detection of poloidal flows (which include meridional flow) requires us to measure the couplings of p modes of distinct l. For instance, mode couplings of l differing by odd integers are sensitive to poloidal velocity patterns of odd s (Lavely & Ritzwoller (1992), Appendix C). These couplings are also sensitive to toroidal patterns, but since the latter are of even s, poloidal and toroidal patterns are in principle distinguishable.

The top panel of Figure 8 shows a composite of time-averaged magnetic (even-s) mode-coupling spectra, computed in an analogous way to the velocity spectra, but using spectra of both odd and even t. The position of the magnetic peak is consistent with well-known observations that solar activity rotates slightly faster than the nominal rotation rate. The excess speed of magnetic features over the speed estimated from line-of-sight velocity and seismic measurements may be a consequence of magnetic features emerging from deeper, faster-rotating layers in the Sun (Snodgrass 1983, 1984; Gilman et al. 1989). For the magnetic analysis the ξ coefficients are simple averages based on p modes within a given frequency range. For Figure 8, the range used was 2.5 to 3.5 mHz. For the range 1.5 to 2.5 mHz, the power in the magnetic peak (not plotted) is about a factor of 10 smaller than the power of the peak shown.

4 DISCUSSION AND OUTLOOK

As indicated in Figures 1 and 2, the statistical model approximately reproduces the observed mode-coupling noise power. However the mismatch between theory and observation is statistically significant and deserves investigation. Possible reasons for the mismatch include systematic errors in the model (e.g., error in the fitted p-mode parameters and/or error in the assumed leakage matrix) or model incompleteness. The present analysis ignored background contributions to the solar oscillation signal, though these contributions are unlikely to be significant except at fairly low oscillation frequencies. The assumption of gaussian wave statistics could, and probably should, be questioned. (In theory the statis-

tics of the solar oscillations should reflect the statistics of the turbulence which drives them.) However, it seems that the problem of testing the gaussian assumption is a difficult one as it is tied to the problem of validating data model parameters.

More rigorous analysis of helioseismic data may help to bridge the significant gap between the noise of MDI mode-coupling measurements and that of ideal measurements (Figure 1). To exploit existing data sets more fully, we want to go beyond the simple $\hat{b}$ analysis and in the direction of the likelihood method sketched in Section 2. This would involve a weighting of covariance data based on their zeroth-order expectation values and 'unfreezing' many parameters whose uncertainty is implicitly neglected in the simple approach. The b parameters that describe the couplings of modes of different l are implicitly assumed to be zero in the simple approach. But they are of interest in themselves and would be included in a more complete analysis. We would also like to model p- and f-mode data at higher l, to sample closer to the surface. At sufficiently high l it becomes necessary to model the effect of differential rotation on mode eigenfunctions. It may also be necessary to compute model couplings using these eigenfunctions.

ACKNOWLEDGEMENTS

This research was supported by NASA grant 80NSSC20K0707 to NWRA/CoRA. MDI data were provided by NASA/*SOHO* and the MDI science team, with technical assistance and valuable inputs from Jesper Schou and Tim Larson. The author thanks an anonymous referee for helpful suggestions.

DATA AVAILABILITY

Data and software generated in this study are available on request.

REFERENCES

Braun D. C., 1995, ApJ, 451, 859
Cally P. S., Moradi H., Rajaguru S. P., 2016, Washington DC American Geophysical Union Geophysical Monograph Series, 216, 489
Fan Y., Braun D. C., Chou D. Y., 1995, ApJ, 451, 877
Featherstone N. A., Haber D. A., Hindman B. W., Toomre J., 2006, in Proceedings of SOHO 18/GONG 2006/HELAS I, Beyond the spherical Sun.
Gilman P. A., Morrow C. A., Deluca E. E., 1989, ApJ, 338, 528
Gizon L., Birch A. C., 2004, ApJ, 614, 472
Greer B. J., Hindman B. W., Featherstone N. A., Toomre J., 2015, ApJ, 803, L17
Hanasoge S. M., Woodard M., Antia H. M., Gizon L., Sreenivasan K. R., 2017, MNRAS, 470, 1404
Larson T. P., Schou J., 2015, Sol. Phys., 290, 3221
Lavely E. M., Ritzwoller M. H., 1992, Royal Society of London Philosophical Transactions Series A, 339, 431
Liang Z.-C., Gizon L., Birch A. C., Duvall T. L., 2019, A&A, 626, A3
Libbrecht K. G., Woodard M. F., 1990, Nature, 345, 779
Lindsey C., Braun D. C., 2000, Science, 287, 1799
Löptien B., Gizon L., Birch A. C., Schou J., Proxauf B., Duvall T. L., Bogart R. S., Christensen U. R., 2018, Nature Astronomy, 2, 568
Mandal K., Hanasoge S., 2020, ApJ, 891, 125 [M20]
Nagashima K., Birch A. C., Schou J., Hindman B. W., Gizon L., 2020, A&A, 633, A109
Proxauf B., Gizon L., Löptien B., Schou J., Birch A. C., Bogart R. S., 2020, A&A, 634, A44
Scherrer P. H., et al., 1995, Sol. Phys., 162, 129
Schou J., 1992, PhD thesis, , Aarhus University, Aarhus, Denmark, (1992) [S92]
Snodgrass H. B., 1983, ApJ, 270, 288
Snodgrass H. B., 1984, Sol. Phys., 94, 13
Woodard M. F., 2007, ApJ, 668, 1189
Woodard M., 2014, Sol. Phys., 289, 1085 [W14]
Woodard M. F., 2016, MNRAS, 460, 3292 [W16]
Woodard M., Schou J., Birch A. C., Larson T. P., 2013, Sol. Phys., 287, 129

This paper has been typeset from a TEX/LATEX file prepared by the author.